ADVANCED FUNCTIONAL MATERIALS

FULL PAPER

DOI: 10.1002/adfm.200700505

Micro Solid Oxide Fuel Cells on Glass Ceramic Substrates**

By *Ulrich P. Muecke, Daniel Beckel, André Bernard, Anja Bieberle-Hütter, Silvio Graf, Anna Infortuna, Patrik Müller, Jennifer L. M. Rupp, Julian Schneider,* and *Ludwig J. Gauckler**

Miniaturized solid oxide fuel cells are fabricated on a photostructurable glass ceramic substrate (Foturan) by thin film and micromachining techniques. The anode is a sputtered platinum film and the cathode is made of a spray pyrolysis (SP)-deposited lanthanum strontium cobalt iron oxide (LSCF), a sputtered platinum film and platinum paste. A single-layer of yttria-stabilized zirconia (YSZ) made by pulsed laser deposition (PLD) and a bilayer of PLD–YSZ and SP–YSZ are used as electrolytes. The total thickness of all layers is less than 1 μm and the cell is a free-standing membrane with a diameter up to 200 μm. The electrolyte resistance and the sum of polarization resistances of the anode and cathode are measured between 400 and 600 °C by impedance spectroscopy and direct current (DC) techniques. The contribution of the electrolyte resistance to the total cell resistance is negligible for all cells. The area-specific polarization resistance of the electrodes decreases for different cathode materials in the order of Pt paste > sputtered Pt > LSCF. The open circuit voltages (OCVs) of the single-layer electrolyte cells ranges from 0.91 to 0.56 V at 550 °C. No electronic leakage in the PLD–YSZ electrolyte is found by in-plane and cross-plane electrical conductivity measurements and the low OCV is attributed to gas leakage through pinholes in the columnar microstructure of the electrolyte. By using a bilayer electrolyte of PLD–YSZ and SP–YSZ, an OCV of 1.06 V is obtained and the maximum power density reaches 152 mW cm^{-2} at 550 °C.

1. Introduction

Power for portable electronic devices, such as, laptops or mobile phones is usually supplied by rechargeable batteries. However, the energy requirements of future devices are projected to increase at a faster rate than the capacity of rechargeable batteries and it becomes difficult to provide reasonable running times without increasing battery size.[1,2] The desire for alternative small-scale energy supplies created substantial interest in miniaturized fuel cells, from which more energy per volume and weight is expected than from batteries.[3,4] Furthermore, they potentially allow instant refueling.

There are currently three types of microfuel cells under investigation: micropolymer electrolyte/proton exchange membrane fuel cells (μ-PEMFCs), microdirect methanol fuel cells (μ-DMFCs), and micro solid oxide fuel cells (μ-SOFCs). The highest power densities of μ-PEMFCs and μ-DMFCs with air as oxidant and hydrogen or diluted methanol as fuel are reported to be 130 mW cm^{-2} at 40 °C and 100 mW cm^{-2} at 60 °C, respectively.[5–10] When oxygen is used at the cathode side, the power density can be improved to 195 mW cm^{-2} at 25 °C for μ-PEMFCs.[11] However, oxygen is not a viable oxidant for portable applications as it has to be provided from a separate tank.

The storage and distribution of pure hydrogen, which is needed as fuel for μ-PEMFCs, is difficult at present and current storage solutions do not scale down efficiently.[12,13] Both μ-PEMFCs and μ-DMFCs also face challenges in water management and thermal control. In μ-DMFCs, methanol cross-over is a fundamental problem and special solutions for pumping the liquid fuel need to be incorporated.[14]

In contrast to the polymer-based fuel cells, SOFCs offer the advantage of running on a variety of fuels like hydrogen or liquefied petroleum gas. The higher energy density of, i. e., butane (7290 W h L_{liquid}^{-1} and 12 600 W h kg^{-1}) compared to hydrogen (2330 W h L_{liquid}^{-1} and 32 900 Wh kg^{-1}) or methanol (4384 W h L^{-1} and 5600 W h kg^{-1}) [8], would offer longer runtimes at the same weight or volume. The theoretical energy density of rechargeable lithium-ion batteries, for comparison, is 410 W h kg^{-1}.[15] μ-SOFC systems are likely to contain a fuel pre-reformer[16] to reduce the coking tendency at the anode by converting the hydrocarbon fuel to syngas,[17] and a post-combustor to oxidize hydrogen and carbon monoxide in the fuel cell exhaust to water and carbon dioxide.[1] The targeted operating temperature of μ-SOFCs is 300–600 °C, which is considerably lower than that of their larger counterparts operating at 800–1 000 °C.

Several studies were conducted on single thin film components for μ-SOFCs, examining their preparation and

[*] Prof. L. J. Gauckler, Dr. U. P. Muecke, Dr. D. Beckel, Dr. A. Bieberle-Hütter, S. Graf, Dr. A. Infortuna, Dr. J. L. M. Rupp, J. Schneider
Department of Materials, Nonmetallic Inorganic Materials
ETH Zurich
Wolfgang-Pauli-Str. 10, 8093 Zurich (Switzerland)
E-mail: ludwig.gauckler@mat.ethz.ch
Prof. A. Bernard, P. Müller
Institute for Micro- and Nanotechnology, NTB
Interstate University of Applied Sciences Buchs
Werdenbergstr. 4, 9471 Buchs (Switzerland)

[**] Financial support from the Commission for Technology and Innovation (grants: KTI 7085.2 DCPP-NM and KTI 8446.1 DCPP-NM), Center of Competence Energy and Mobility (CCEM), Bundesamt für Energie (BfE), Swiss Electric Research and European Union within the REAL-SOFC project is gratefully acknowledged.

ADVANCED FUNCTIONAL MATERIALS

microstructure,[18–29] electrical and electrochemical properties,[18,25,27,30–39] and suitability for application in a μ-SOFC. However, only a few studies were dedicated to modeling[40,41] and fabrication of entire μ-SOFCs.[42–44]

One main result from modeling was that the electrodes are expected to limit the performance of the cell. Fleig et al.[40] concluded that reduction of the electrolyte thickness below the particle-to-particle distance of the electrode materials does not lead to a significant reduction of electrolyte resistance due to current constrictions in the electrolyte. This emphasizes the importance of the electrode microstructure and suggests either the use of electrodes with nanometer-sized grains or dense electrodes of a mixed ionic–electronic conductor.[45–47] It was also found experimentally that the electrodes limit the performance of μ-SOFCs.[42] The electrode resistance was found to be one order of magnitude larger than that of the electrolyte, attributed mainly to the cathode.

All μ-SOFCs reported in the literature up to now were built up on silicon[42] or metallic nickel substrates.[43,44] In this work, Foturan, a photostructurable silica-based glass ceramic that can be micromachined by etching with hydrofluoric acid, was used.[48] The parts to be removed are first irradiated with UV light and then crystallized at temperatures of 500–600 °C. The crystallized areas are attacked ~20 times faster by HF than the amorphous matrix and dissolve during the HF treatment. Foturan is a suitable substrate for μ-SOFC application, since its thermal expansion coefficients of 8.6×10^{-6} K^{-1} in the glassy state and 10.5×10^{-6} K^{-1} in the crystalline state[49] match well with the other SOFC materials.

The aim of this paper is to demonstrate the feasibility of μ-SOFCs on a glass ceramic substrate. The current–voltage (*I–V*) characteristics and power densities of microfabricated cells are reported. The polarization resistance of metallically and mixed ionic–electronically conducting cathode materials was evaluated by impedance spectroscopy and direct current (DC) techniques and the influence of electrode and electrolyte microstructure on cell performance was studied.

2. Results and Discussion

2.1. Microstructure of Sputtered Platinum Electrodes

Figure 1 compares the microstructures of two identically prepared sputtered Pt films with a thickness of 35–50 nm on the anode (Fig. 1a) and on the cathode (Fig. 1b) side of a μ-SOFC after testing. Both films were exposed to the same maximum temperature of 600 °C. The average grain and pore size of the film on the anode side was several times larger than those on the cathode side. Adhesion to the electrolyte was very good and no delamination was observed.

The porosity of the anode film evolved during two stages of the cell preparation. During the Foturan crystallization at 600 °C for 1 h, the film was sandwiched between the substrate material and the yttria-stabilized zirconia (YSZ) electrolyte in a fixed gap and only some small pores formed. However, after removal of the Foturan substrate, coarsening of the Pt was observed after exposure to hydrogen/nitrogen at 600 °C and a film with pore sizes in the 100–500 nm range was formed. The cathode film also coarsened at 600 °C in air, but the pore size remained in the 20–200 nm range. Lowering the maximum operating temperature resulted in a finer microstructure and lower polarization resistances of both films.

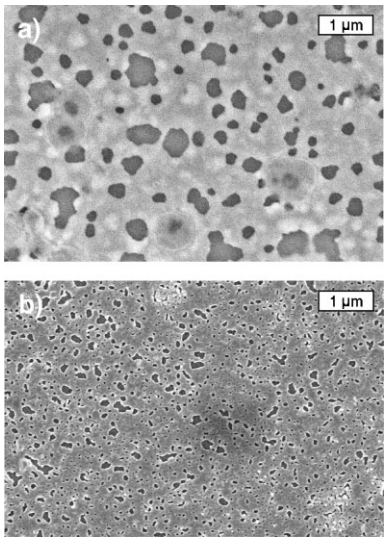

Figure 1. SEM top-view images of 35–50 nm sputtered Pt thin film after testing at 600 °C: a) anode thin film after 30 min under reducing conditions and b) cathode film after 1 h in air. The dark areas are pores.

Accelerated grain growth of platinum under hydrogen with detrimental effects on electrode performance was also observed by Vanherle and McEvoy.[50] The electrochemical reactions at metallic electrodes are confined to the vicinity of the triple phase boundary if the metal does not conduct an electrochemically active species.[51] This assumption is valid for platinum at the cathode side[52] and, although Pt is permeable for hydrogen, also valid at the anode side because only a limited amount of water can be formed underneath the Pt film. The triple phase boundary length per electrode unit area and, accordingly, the microstructure/porosity of the electrodes determine the electrochemical activity of a thin film metal electrode. The maximum triple phase boundary length and with it the highest catalytic activity can, therefore, be achieved with platinum electrodes annealed no higher than the operating temperature of the fuel cell. However, grain coarsening during operation then causes an increase in polarization resistance over time. The thermal stability of the platinum film, therefore, is setting a lower limit for the polarization resistance of pure platinum electrodes, especially for platinum anodes.

2.2. Microstructure of Chromium/Platinum Anode Contacts

The Cr/Pt anode contacts showed no signs of porosity after testing at 600 °C if the thickness exceeded ~100 nm. The films were sputtered at higher energies compared to the anode and

cathode thin films and were denser after deposition. Films thinner than 100 nm were stable only if sandwiched between Foturan and an electrolyte film, and developed some pores in areas exposed to air. So, the deposition process also has an influence on the evolution of porosity in Pt films during annealing. The films adhered very well to the Foturan surface and delamination was never observed.

2.3. Influence of Cathode Material on Fuel Cell Performance

2.3.1. Platinum Paste Cathode: The simplest μ-SOFC consisted of a 200 nm sputtered Pt anode, a 550 nm PLD–YSZ film and a 10–20 μm Pt paste cathode covering the membrane area. In this configuration, the thin film cell is supported by the metal paste covering the membrane, which was initially believed to be detrimental to membrane stability because of the different thermal expansion coefficients of Pt and YSZ. However, the membranes proved to be crack-free after testing and Pt could be used as cathode. The PLD electrolyte was dense, columnar, and crack-free after testing (Fig. 2a).

Impedance spectra and *I–V* curves of the cell were recorded between 600 and 400 °C. The anode gas was dry 1:4 H_2/N_2. The OCVs of a representative cell were 0.91, 0.9, and 0.81 V and the power densities 14.7, 1.7, and 0.11 mW cm^{-2} at 600, 500, and 400 °C, respectively (Fig. 3a). No difference in OCV between dry and humidified fuel was observed, indicating that water was produced at the anode/electrolyte interface due to gas leakage (details see below). The electrode polarization resistance $R_A + R_C$ was 60 Ω · cm^2 at 550 °C with an activation energy of 1.0 eV (Fig. 4). The electrolyte resistance R_Ω was 0.054 Ω · cm^2 at 550 °C and negligible compared to the electrode resistance. The cell performance was, therefore, limited by the electrodes.

The electrolyte resistance corresponded to a conductivity of 0.07 S m^{-1} at 550 °C and agreed well with in-plane values of 0.065 S m^{-1}[53] for identically prepared PLD–YSZ films (also plotted in Fig. 4 for comparison). The electrolyte activation energy of 0.92 eV also fit well to the literature value of 1.02 eV.

Analysis of the cells after testing showed that the Pt paste exhibited a coarse microstructure with a grain size of 100–200 nm and pores in the 0.5–1 μm range at the cathode/electrolyte interface (Fig. 1a and b). The paste adhered poorly to the electrolyte surface, resulting in a large polarization resistance of the cathode.

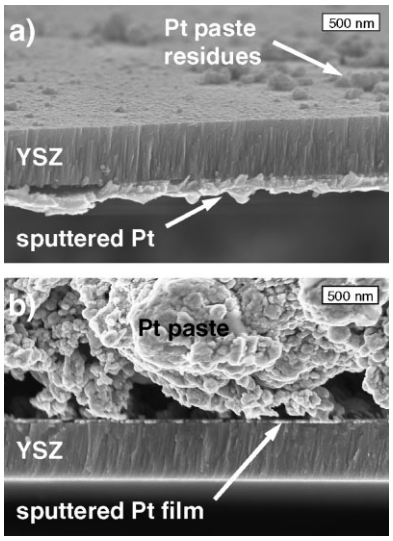

Figure 2. SEM cross-sectional images of a) a free-standing sputtered Pt/PLD YSZ/Pt paste membrane. The Pt paste detached during breaking of the sample. b) SEM cross-sectional view of the PLD–YSZ/sputtered Pt/Pt paste interface adjacent to the fuel cell membrane.

2.3.2. Sputtered Platinum Cathode: To increase the cell performance, the platinum paste cathode was replaced with a 35–50 nm thick sputtered platinum thin film cathode. The anode and electrolyte remained unchanged, except that the anode thickness was decreased to 35–50 nm. The Pt paste cathode contact was placed adjacent to the membrane and the fuel cell itself was free-standing without Pt paste support.

The sputtered Pt film formed a well-connected 2D porous structure with pore sizes below 200 nm and had a finer microstructure than the platinum paste cathode (Fig. 2b). The number of contact points to the electrolyte surface increased in comparison to the Pt paste (Fig. 1) and the film adhered well to the electrolyte surface.

The OCV of a representative cell ranged from 0.66 to 0.77 V with dry 1:4 H_2/N_2 as fuel and the power densities were 26.4,

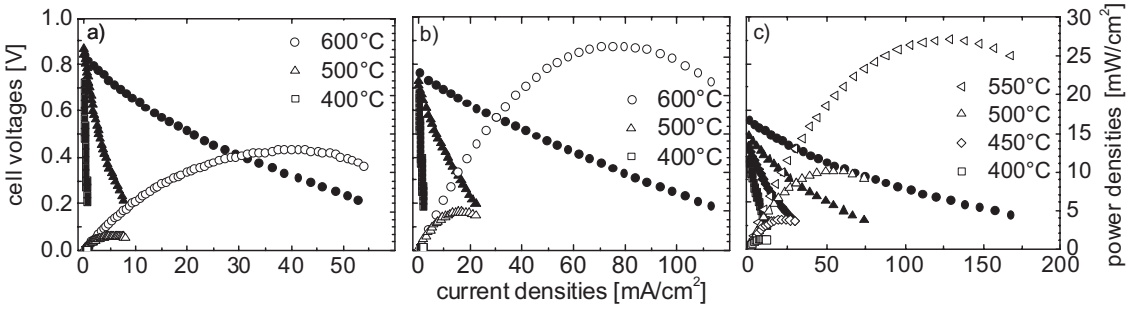

Figure 3. Current–voltage curves of cells with a sputtered Pt anode, a PLD–YSZ electrolyte and different cathode materials: a) Pt paste, b) sputtered Pt, and c) LSCF.

ADVANCED FUNCTIONAL MATERIALS

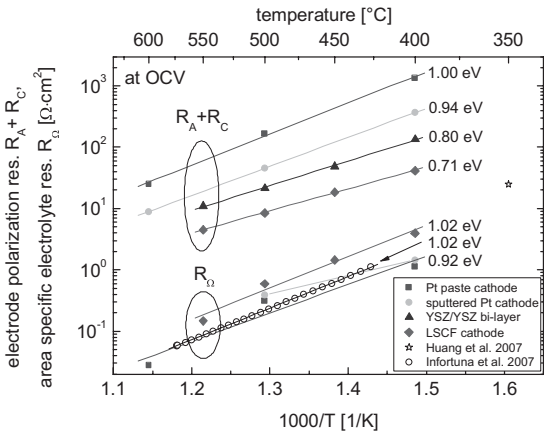

Figure 4. Arrhenius plot of the electrode polarization resistances $R_A + R_C$ and area-specific electrolyte resistances R_Ω for single-layer electrolyte cells with different cathode materials and a bilayer electrolyte cell. Literature values were taken from references [42] and [53].

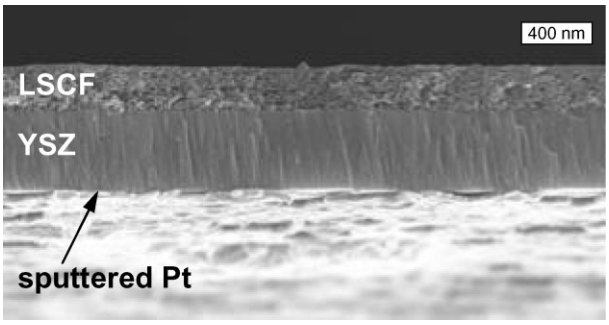

Figure 5. SEM cross-sectional image of a free-standing μ-SOFC membrane with sputtered Pt anode, PLD–YSZ electrolyte, and sprayed LSCF cathode after testing.

4.9, and 0.43 mW cm^{-2} at 600, 500, and 400 °C, respectively (Fig. 3b). The electrode polarization resistance was 19 $\Omega \cdot cm^2$ at 550 °C (Fig. 4) and approximately a factor of 3 lower than that for the Pt paste cathode, indicating that the cathode was rate limiting. The electrode activation energy of 0.94 eV was roughly equal to that of the Pt paste cathode cell (1.0 eV). The electrolyte resistance remained unchanged within experimental errors (Fig. 4) and was still negligible compared to the electrode resistance.

2.3.3. Lanthanum Strontium Cobalt Iron Oxide (LSCF) Cathode by Spray Pyrolysis (SP): To eliminate the expensive precious metal at the cathode side, cells with a fully ceramic perovskite cathode were prepared. Based on the report of Beckel et al.,[27] showing cathode polarization resistances as low as 7.2 $\Omega \cdot cm^2$ at 550 °C for LSCF thin films made by SP, a 200–250 nm thick LSCF cathode film on top of the YSZ electrolyte was incorporated in the cell.

LSCF in contact with YSZ is known to form lanthanum or strontium zirconates at elevated temperatures. However, as the maximum processing temperature of the μ-SOFC did not exceed 600 °C for 1 h, the zirconate formation is kinetically hindered and only expected after prolonged operating times.[54,55]

The membrane with a diameter of 200 μm was free standing and the LSCF cathode was contacted by a Pt paste dot adjacent to the membrane. The LSCF formed a very homogeneous nanoporous structure with an average grain size of ~20 nm, as observed in scanning electron microscopy (SEM) cross-sectional micrographs, and adhered well to the YSZ electrolyte (Fig. 5).

The OCV of 15 different cells with LSCF cathodes ranged from 400 to 913 mV at 550 °C. Current–voltage curves of a representative cell are shown in Figure 3c. The power densities with dry 1:4 H_2/N_2 fuel were 27.1, 10.1, 3.8, and 1.3 mW cm^{-2} (Fig. 3c) and the electrode polarization resistances were 4.5, 8.4, 18.4, and 41.5 $\Omega \cdot cm^2$ at 550, 500, 450, and 400 °C, respectively (Fig. 4). Although, the OCV was lower than that of the Pt cathode cells, the power density at 550 °C was the same as that of the sputtered Pt cathode cell at 600 °C. The electrode activation energy of 0.71 eV was lower than that of the Pt cathode cells with 0.94–1.0 eV, which resulted in higher power densities toward lower temperatures.

The total electrode polarization resistance with LSCF cathodes was the lowest achieved in this work and shows that the performance of the cells can be increased by using a perovskite cathode.

2.4. Open Circuit Voltage

The OCVs of over 30 tested cells with PLD–YSZ electrolytes always fell within the range of 400–900 mV in the temperature range of 400–600 °C, regardless of the cathode material used. OCVs lower than the theoretical value are usually observed in SOFCs with the presence of cracks, pores, or pinholes in the electrolyte or if the electrolyte material is electronically conductive. Cracks could be excluded by SEM examination of the membranes after testing. Although, bulk YSZ is regarded as a purely ionic conductor below 1000 °C and within the oxygen partial pressure range used in SOFCs, the electrical conductivity of nanograined YSZ thin films might differ from the bulk material. The cross-plane electrical conductivity of a supported PLD–YSZ electrolyte film was, therefore, measured in air and under reducing conditions to check for electronic conductivity.

The cross-plane conductivity of the PLD–YSZ film was 0.019 S m^{-1} with an activation energy of 1.05 eV in air, and 0.016 S m^{-1} with an activation energy of 1.07 eV in dry H_2/N_2 at 400 °C (Fig. 6). The cross-plane conductivity in air was a factor of 8 higher than the in-plane conductivity of an identically prepared film on sapphire (2.4×10^{-3} S m^{-1}).[53] The differences between in-plane and cross-plane measurements might be attributed to the columnar microstructure of the films under the assumption of low conductivity grain boundaries.[56] The literature values for the electrical conductivities of nanocrystalline YSZ scatter by roughly one order of magnitude, depending on the preparation method, grain size, microstructure, etc. However, activation energies of micro-

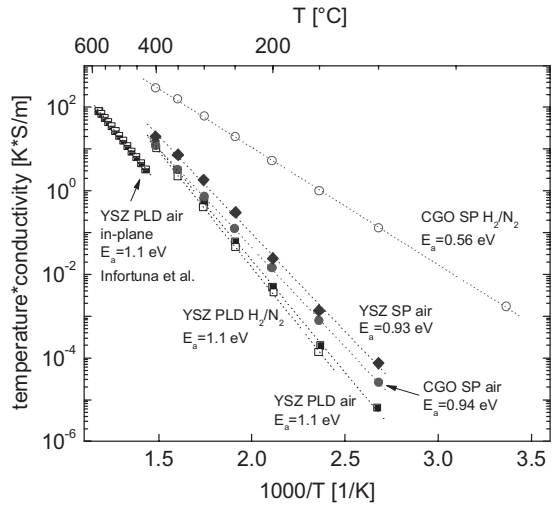

Figure 6. Arrhenius plot of the in-plane and cross-plane conductivity of various electrolyte thin films in air and under reducing conditions. The in-plane data of the PLD–YSZ film were taken from. [53]

and nanocrystalline samples are usually around 1 eV,[57–60] which fits well with the value reported here.

The cross-plane conductivity of YSZ and cerium gadolinium oxide (CGO) electrolyte films prepared by SP are also given in Figure 6 for comparison. The cross-plane conductivity in air of the SP–YSZ film was 0.03 S M^{-1} at 400 °C with an activation energy of 0.93 eV, and that of the SP–CGO film in air was 0.018 S m^{-1} with an activation energy of 0.94 eV. The low conductivity of the CGO films can be attributed to the nanocrystalline microstructure,[25] whereas conductivity values comparable to bulk samples are observed for nanocrystalline YSZ films.[61,62] After the exposure to a reducing atmosphere, the SP–CGO films were predominantly electronic conductors between 400 °C and room temperature, which can be explained by the shift of the electrolytic domain boundary toward higher oxygen partial pressures for nanocrystalline CGO.[25] The high electronic conductivity of the nanocrystalline SP–CGO films, therefore, prevents the use as single-layer electrolytes in μ-SOFCs but makes them suitable candidates as cathodic buffer layers to prevent lanthanum zirconate formation between YSZ and LSCF.

No change in conductivity or activation energy between room temperature and 400 °C was detected for the PLD–YSZ film upon exposure to a reducing atmosphere (see Fig. 6). These results suggest that the reduced OCV of the cells was caused by gas diffusion through pores or pinholes and not by an increased electronic leakage through the electrolyte under reducing conditions. Pinholes in sputtered electrolyte films were already reported by others[63–65] and were associated with the columnar microstructure of the films. The pinhole diameter of radio frequency (RF) sputtered YSZ was given as 50–200 nm for an electrolyte thicknesses of 4 μm by Kleinlogel[63] and OCVs as low as 200 mV were reported for cells with these electrolytes. When the electrolyte thickness is reduced to 500–600 nm, diffusion is expected to be even higher due to the shorter diffusion length and consequently larger concentration gradient.

The PLD–YSZ electrolyte in this study also exhibited a columnar microstructure with single grains extending through the complete thickness of the film (Fig. 2a, 2b, and 5). Small gaps between adjacent columns or small voids at the triple junctions with sizes less than 10 nm were observed in SEM top view micrographs (marked in Fig. 7). The lower-than-theoretical OCVs were hence ascribed to gas diffusion through very small pores and pinholes in the columnar microstructure of the PLD films.

2.5. Bilayer Electrolyte Cell

Consequently, a dense 200 nm SP–YSZ film was applied on top of the PLD–YSZ film to seal the pinholes in the PLD–YSZ film. The average grain size of the SP–YSZ film was 10 ± 5 nm after the Foturan crystallization at 600 °C for 1 h (Fig. 8). No distinct interface between the PLD–YSZ and SP–YSZ film was visible, indicating good adhesion of the two films. Sputtered 35–50 nm platinum was used as an anode and platinum paste was used as the cathode material for the sake of simplicity.

The OCV of the cell with a 3 vol % humidified 1:4 H_2/N_2 fuel ranged from 1.04 to 1.06 V, which corresponds well to the theoretical OCV of 1.087 V at 550 °C calculated with the Nernst equation.[66] The power densities were 152, 56.5, 16.6, and 3.8 mW cm^{-2} at 550, 500, 450, and 400 °C, respectively (Fig. 9) and the electrode polarization resistance was 11 $\Omega \cdot cm^2$ at 550 °C (Fig. 4) with an activation energy of 0.8 eV. Although, the cathode was not optimized, the maximum power density was in the same range or higher than literature values of μ-PEMFCs, μ-DMFCs, or silicon-based μ-SOFCs operating at the same temperature. For the latter, Jankowski et al.[67] measured 73 mW cm^{-2} at 550 °C with a nickel/YSZ/silver cell, and Chen et al.[43] reported 90 mW cm^{-2} at 550 °C with a

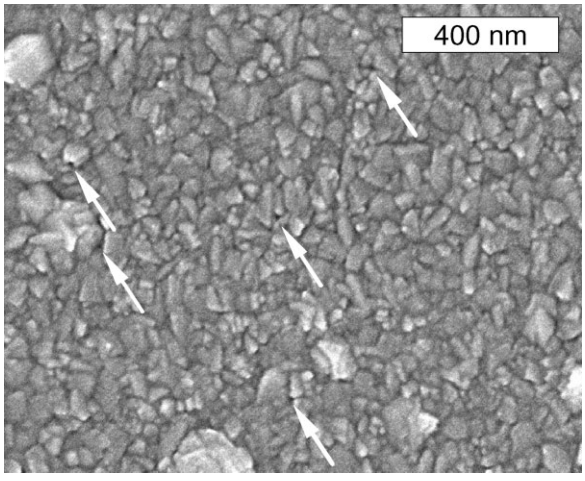

Figure 7. SEM top-view image of a PLD–YSZ electrolyte film after testing at 550 °C in air. Possible pinholes are marked with arrows.

ADVANCED FUNCTIONAL MATERIALS

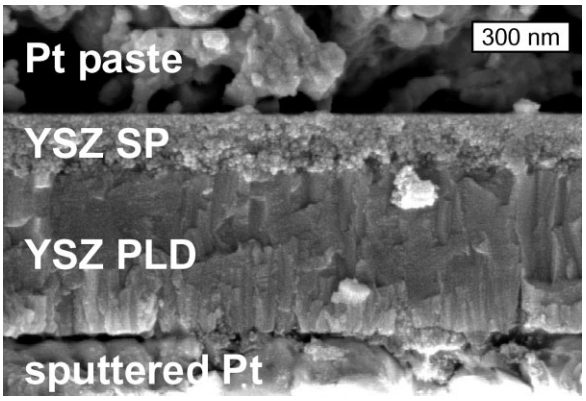

Figure 8. SEM cross-sectional image of a bilayer PLD–YSZ/SP–YSZ electrolyte cell with sputtered Pt anode and Pt paste cathode after testing.

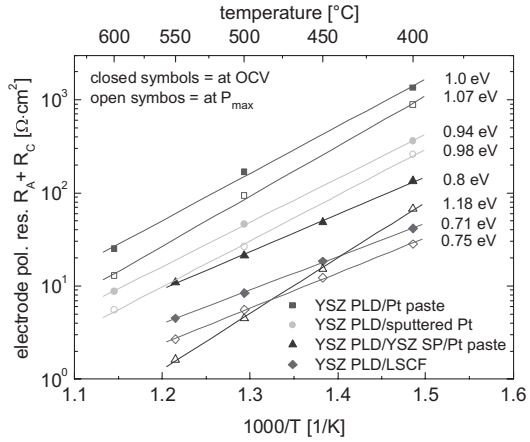

Figure 10. Arrhenius plot of electrode polarization resistances of all cells at OCV and at the voltage of maximum power output P_{max}.

Ni-YSZ/YSZ/lanthanum strontium cobaltite cell. Huang et al.[42] reported performance data up to 400 °C and found power densities of 400 mW cm^{-2} at 400 °C with a Pt/YSZ/CGO/Pt cell. The good performance was attributed to the fine microstructure of the platinum electrodes and the CGO interlayer. At higher temperatures, however, coarsening of the fine-grained Pt electrodes is expected.

Microtubular fuel cells with diameters in the millimeter range reached power densities of 350 mW cm^{-2} at 550 °C,[68] 450 mW cm^{-2} at 550 °C,[69] and 740 mW cm^{-2} at 650 °C.[70] However, the wall thickness of the tubes is in the range of 200–300 μm and the cells are more comparable to state-of-the-art anode supported SOFCs than to thin film cells. Electrolyte supported miniaturized single chamber SOFCs with electrode thicknesses of ~10 μm showed a power density of 17 mW cm^{-2} at 650 °C,[71] and anode supported single chamber cells with electrolyte and electrode thicknesses of 10–30 μm 250 mW cm^{-2} at 600 °C.

The *I–V* curves of the cell in this study showed activation polarization at low current densities and a near-constant slope thereafter (Fig. 9). Activation polarization was less pronounced in the single-layer electrolyte cells with OCVs

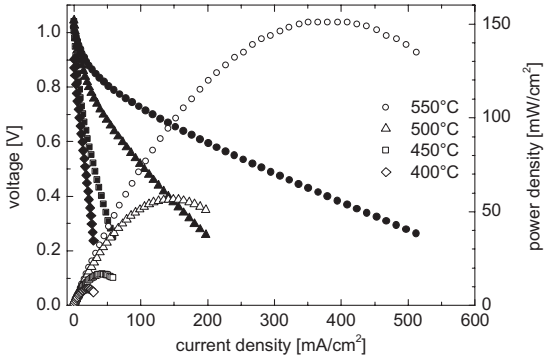

Figure 9. Current–voltage curve of a cell with sputtered platinum anode, PLD–YSZ and SP–YSZ bilayer electrolyte and platinum paste cathode.

below the theoretical value. The comparison of electrode polarization resistances at open circuit conditions with different levels of activation polarization might, therefore, lead to misinterpretations of the electrode performance. Thus, the electrode polarization resistances $R_A + R_C$ at OCV conditions were additionally compared to the values obtained from the *I–V* curve at maximum power P_{max}. Because the voltage drop across the electrolyte is negligible, the value of $R_A + R_C$ at P_{max} can be calculated from the cell voltage U at P_{max} and the current density i at P_{max} as $R_A + R_C = (OCV - U)/i$. The same formula can be used to calculate the electrode polarization resistance or the electrode overpotential at any point of the current–voltage curves.

The electrode resistances at P_{max} were approximately a factor of 2 smaller than at OCV conditions for all single-layer electrolyte cells with low activation polarization and the activation energy changed by less than 10% (Fig. 10). However, an increase in activation energy from 0.8 eV at OCV to 1.18 eV at P_{max} and a drop of resistance by roughly a factor of seven from 11 to 1.63 Ω · cm^2 at 550 °C was found for the bilayer electrolyte cell with strong activation polarization. The comparison of electrode polarization resistance at open circuit conditions can, therefore, lead to an underestimation of the cell performance.

The sprayed electrolyte film additionally improved the cathode/electrolyte interface, and the electrode resistance at P_{max} of the bilayer cell with Pt paste cathode was lower than that of the LSCF cathode cells at P_{max}. The cell performance might again be improved by using an YSZ/YSZ or YSZ/CGO bilayer electrolyte together with an LSCF cathode. These cells are currently under investigation in our laboratory.

3. Conclusions

The feasibility of fabricating miniaturized solid oxide fuel cells on photostructurable glass ceramic substrates was successfully demonstrated for the first time. The cells were

prepared by thin film techniques with a maximum processing temperature of 600 °C. Sputtered Pt was used as an anode; single- or bilayer YSZ as an electrolyte; and Pt paste, sputtered Pt or LSCF as a cathode. The fuel cells themselves were free-standing membranes of less than 1 μm thickness and with diameters up to 200 μm. All fuel cell membranes were crack-free after electrochemical testing at 600 °C.

It was shown that the choice of cathode material and the gas-tightness of the electrolyte determined the cell performance. The electrode polarization resistances of a single-layer PLD–YSZ cell decreased based on the cathode material in the order Pt paste, sputtered Pt then LSCF, with LSCF cathode cells showing the highest power density.

Lower-than-theoretical open circuit voltages (OCVs) were measured for all cells with single-layer PLD–YSZ electrolyte. The low open circuit potentials were attributed to gas leakage through the columnar PLD–YSZ electrolyte after electronic conductivity of the electrolyte was excluded by cross-plane conductivity measurements under reducing conditions.

The best cell performance was measured on a cell with sputtered platinum anode, bilayer YSZ electrolyte prepared by pulsed laser deposition (PLD) and SP, and a platinum paste cathode. Theoretical OCV of 1.06 V and a maximum power density of 152 mW cm^{-2} at 550 °C were achieved.

4. Experimental

The following section gives an overview of the thin film deposition procedures used for the anode, electrolyte, and cathode, followed by the steps necessary to fabricate a miniaturized SOFC. The anode, electrolyte, and cathode of the cells were deposited by sputtering, PLD or air blast SP.

4.1. Thin Film Anode, Cathode, and Electrolyte Preparation

Sputtered Platinum Anode and Cathode: A sputter coater (SCD 050, Balzers, FL) was used to deposit platinum films that were used as anodes and for some cells also as cathodes. The deposition was carried out at room temperature, the gas pressure was 0.05 mbar Ar, the sputter current 60 Ma, and the deposition times were 170 and 680 s, resulting in films with 35–50 and ~200 nm thicknesses, respectively.

Spray Pyrolysis (SP) of LSCF Cathode: The SP setup used to deposit the LSCF cathode is described in detail elsewhere.[26] The working distance was 20 cm, the air pressure 1.0 bar, the precursor flow rate 15 mL h^{-1}, and the substrate surface temperature 280 °C. The deposition time was 30 min, resulting in a film thickness of 200–250 nm.

$La(NO_3)_3 \cdot 6H_2O$ (99%, ABCR, Karlsruhe, DE), $SrCl_2 \cdot 6H_2O$ (99%, Fluka, Buchs, CH), $Co(NO_3)_2 \cdot 6H_2O$ (98%, Alfa Aesar, Karlsruhe, DE, and Fluka), and $Fe(NO_3)_3 \cdot 9H_2O$ (98%, Fluka) were used to prepare the precursor. The salts were mixed in a cation ratio of 3:2:1:4 La/Sr/Co/Fe to obtain a cathode stoichiometry of $La_{0.6}Sr_{0.4}Co_{0.2}Fe_{0.8}O_3$ after deposition. A mixture of ethanol (99.5%, Scharlau, Barcelona, ES) and diethylene glycol monobutyl ether (99%, Acros, Scheel, BE) in a volume ratio of 1:2 was used as a solvent. The total salt concentration was 0.04 mol L^{-1}.

Pulsed Laser Deposition (PLD) of YSZ Electrolyte: YSZ electrolyte films were deposited by PLD (PLD workstation, Surface, Hückelhoven, DE) from a $(Y_2O_3)_{0.08}(ZrO_2)_{0.92}$ target with a 248 nm excimer laser with 4 J cm^{-2} fluence. The target-to-substrate distance was 8.5 cm, the chamber pressure 2.66 Pa oxygen, and the substrate temperature was 400 °C. Fifty-four thousand pulses at a rate of 10 Hz resulted in ~550 nm thick films. The target preparation is described elsewhere.[53]

Spray Pyrolysis of YSZ and CGO electrolyte: A detailed description of the SP setup used to deposit the $(Y_2O_3)_{0.08}(ZrO_2)_{0.92}$ and $Ce_{0.8}Gd_{0.2}O_{1.9-x}$ SP electrolyte was given earlier.[24] The working distance was 39 cm, the air pressure 1.0 bar, the precursor flow rate 2.5 mL h^{-1}, and the substrate surface temperature 410 °C. The deposition time was 60 min, resulting in a film thickness of 500 ± 100 nm.

The precursor for the YSZ films was prepared by dissolving zirconium-(IV)-acetylacetonate (96% purity, Fluka) and yttrium-(III)-chloride hexahydrate (99.9%, Alfa Aesar) with the corresponding stoichiometry in a mixture of 10:10:90 vol % ethanol (99.5%, Scharlau): polyethylene glycol 600 (purum, Fluka): tetraethylene glycol (99%, Aldrich, Steinheim, DE). The polyethylene glycol was added after the complete dissolution of the salts in the ethanol/tetraethylene glycol mixture at 50–80 °C. The total salt concentration was 0.05 mol L^{-1}. Cerium-(III)-nitrate hexahydrate (99.5%, Alfa Aesar) and gadolinium-(III)-chloride hexahydrate (99.9%, Alfa Aesar) were dissolved in a mixture of 10:90 vol % ethanol/tetraethylene glycol at a total salt concentration of 0.1 mol L^{-1} for the preparation of the CGO precursor. The crystal water content of the salts was verified by thermogravimetry before weighing.

4.2. Preparation of Thin Film SOFCs

The miniaturized SOFC was built up on one side of a photostructurable glass ceramic substrate by sequential thin film deposition of anode contacts, anode, electrolyte, and cathode. Four inch Foturan wafers (Mikroglas, Mainz, Germany) with 300 μm thickness and polished on both sides were used as substrates. After the thin film deposition, a small portion of the substrate was back-etched to create the free-standing fuel cell membrane. The detailed process steps are given in the following.

Alignment Marks: Alignment marks were etched in the backside of the wafer to position all photolithography and shadow masks during cell fabrication (Scheme 1a). The alignment marks were defined using standard photolithography: 1 min spinning of Shipley Microposit S 1813 photoresist at 3000 rpm, 1 min pre-bake at 115 °C, 150 J cm^{-2} light exposure through a mask, developing for about 1 min in Microposit MF 321 developer. The 1–2 μm deep marks were isotropically etched for 5 min using buffered HF.

Chromium/Platinum Anode Contacts: Platinum anode contacts with a thickness of 100 nm were RF sputtered (custom made sputter machine, 100 W, 80 mm working distance, room temperature) through a 0.3 mm-thick Mo mask on the front side of the wafer. A sputtered chromium layer of 30 nm was used as an adhesion layer between the substrate and the platinum film. Circular holes with 100 and 200 μm diameters were patterned in the center of the contacts by lift-off with an aluminum mask. The fuel cells were later going to be at the position of the holes. The aluminum mask was prepared by sputtering a 2 μm Al film (BAS 450, Balzers, LI, room temperature, 1 kW sputter power, 64 min sputter time, 3×10^{-3} mbar Ar pressure) and patterning with the same photolithography process as for the alignment marks (Scheme 1b–d). A mixture of 85 mass % aqueous phosphoric acid and 65 mass % aqueous nitric acid in a volume ratio of 25:1 was used as the aluminum etchant. The aluminum mask was used to prevent ridges at the edge of the sputtered platinum film after lift-off.

UV Irradiation of the Substrate and Cutting of the Wafer: After the deposition of the anode contacts, the wafer was irradiated with UV light (Electronic Visions Group AL 6-2, Schärding, AT, 312 nm, 60 min, 1000 W) through a shadow mask that covered the wafer outside the chromium/platinum anode contacts (Scheme 1e). The holes in the Cr/Pt contacts served as masks for irradiating the cylindrical parts of

ADVANCED FUNCTIONAL MATERIALS

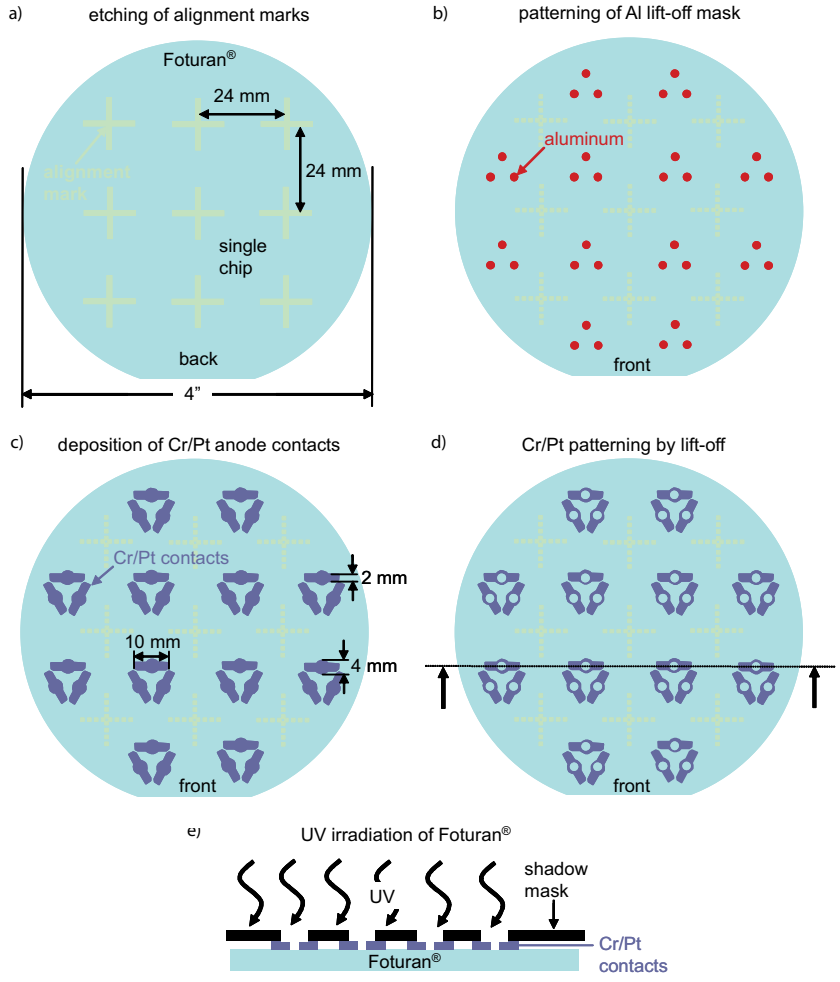

Scheme 1. Wafer processing used to prepare several chips on a substrate. Drawings not to scale.

the substrate that were later back-etched to release the individual fuel cells.

After irradiation, the wafer was cut (DAD 321, Disco, Munich, DE) along the alignment marks into twelve 24 mm × 24 mm chips with three cells per chip.

Deposition of Fuel Cell Layers: The anode, electrolyte, and cathode thin films were sequentially deposited on top of the anode contacts through laser-cut shadow masks of 0.1 mm thickness as depicted in Scheme 2a–c. The anode was deposited through a mask with 3 mm diameter, the electrolyte through a mask with 6 mm diameter, and the cathode through a mask with 0.5 mm diameter. Mo masks were used for sputtering and SP, whereas stainless steel masks were used for all PLD layers to prevent Mo contamination of the films. No temperature treatment of the films was performed between depositions.

Etching: After the thin film deposition, the chips were heated to 500 and 600 °C for 1 h each with 1 °C min^{-1} heating and cooling rates in order to crystallize the UV irradiated areas of the substrate and the fuel cell layers. The chips were sandwiched between two polished alumina plates with a pressure of 22 N cm^{-2} during annealing to prevent warping of the substrate. After annealing, the substrate showed a clear contrast between the brownish, crystalline areas where the holes were to be created and the surrounding transparent glassy areas.

To remove water deposited by handling, the chips were heated to 120 °C for 30 min and subsequently a protective coating (FSC-H, Rohm and Haas, Coventry, UK, 45 min pre-bake at 100 °C) was brushed on the thin film side of the substrate to protect the films against HF attack (Scheme 2d). The crystalline areas of the substrate were then removed in a 10% aqueous solution of HF (diluted from 40% HF, suprapur, Merck, Darmstadt, DE, not buffered) under constant stirring. The average etch time was 22 min for 100 μm diameter membranes and 17 min for 200 μm membranes. The protective coating was removed with acetone after etching and the chips were rinsed with water. A schematic of the cell after processing is shown in Scheme 2e.

Contacting: For electrochemical testing, platinum wires of 127 μm diameter were flat pressed and attached on both sides of the chromium/platinum anode contacts with Pt paste (C3605 P, Heraeus, Hanau, DE) as anode current and voltage leads (Scheme 3). The cathode contact wire was prepared by flat-pressing an 80 μm-diameter Pt wire, bending the first ~0.5 mm of the wire by 90° and dipping the wire tip in platinum paste. For cells with Pt paste cathodes, the tip was positioned on the surface of the electrolyte at the position of the fuel cell, covering the entire area of the membrane. In the case of sputtered Pt and LSCF cathodes, the contact was placed adjacent to the membrane on top of the cathode material, and it was assumed that the Pt or LSCF has sufficient in-plane conductivity to extend the contact over the membrane area. The areas of the circular Pt paste dots were between 0.01 and 0.1 mm^2. All contact wires were attached to the Foturan substrate with ceramic glue (Ceramabond 503, Aremco, Valley Cottage, NY, USA).

Cross-plane Conductivity Measurements of Single Electrolyte Films Supported on a Substrate: The electrical conductivity of single electrolyte films was measured perpendicular to the film surface by impedance spectroscopy. A piece of blank 24 mm ×24 mm Foturan was coated with a Cr/Pt bottom contact layer as described above in the section "Chromium/Platinum anodes contacts", and a 6 mm-diameter circular spot of PLD–YSZ with 550 nm thickness, SP–YSZ with 500 ± 100 nm, or SP–CGO with 500 ± 100 nm was applied on top. After the film deposition, the PLD–YSZ samples were annealed at 600 °C for 1 h, the SP–YSZ and SP–CGO at 600 °C for 10 h, all in air with 3 °C min^{-1} heating and cooling rates, resulting in an average grain size of 10 ± 5 and 15 ± 5 for the SP–YSZ and SP–CGO films, respectively. Platinum top contacts with 5, 1, 0.5, 0.2, and 0.1 mm^2 areas and a thickness of 70–100 nm were then sputtered on top of the film as described above in the section "Sputtered Platinum Anode and Cathode". The bottom Cr/Pt contacts as well as the top Pt areas were contacted with a Pt paste dot and two wires for voltage and current each. All films and contacts were supported by the substrate and no etching was performed.

Impedance spectra of each contact were recorded in air and in dry 1:4 H_2/N_2 in the frequency range from 4 MHz to 0.1 Hz (IM6, Zahner, Kronach, DE). The spectra showed one high frequency arc in the 100 kHz–4 MHz range and one distinctly separated low frequency feature down to 0.1–1 Hz. The high frequency arc was attributed to the electrolyte because its resistance was independent of the DC bias and scaled linearly with the electrolyte thickness. The low frequency arc was attributed to the electrodes. Reproducibility of the conductivity data between samples and from contact to contact was better than 10%.

Characterization: The sample microstructures were analyzed with a SEM(LEO 1530, Carl Zeiss SMT, Oberkochen, DE).

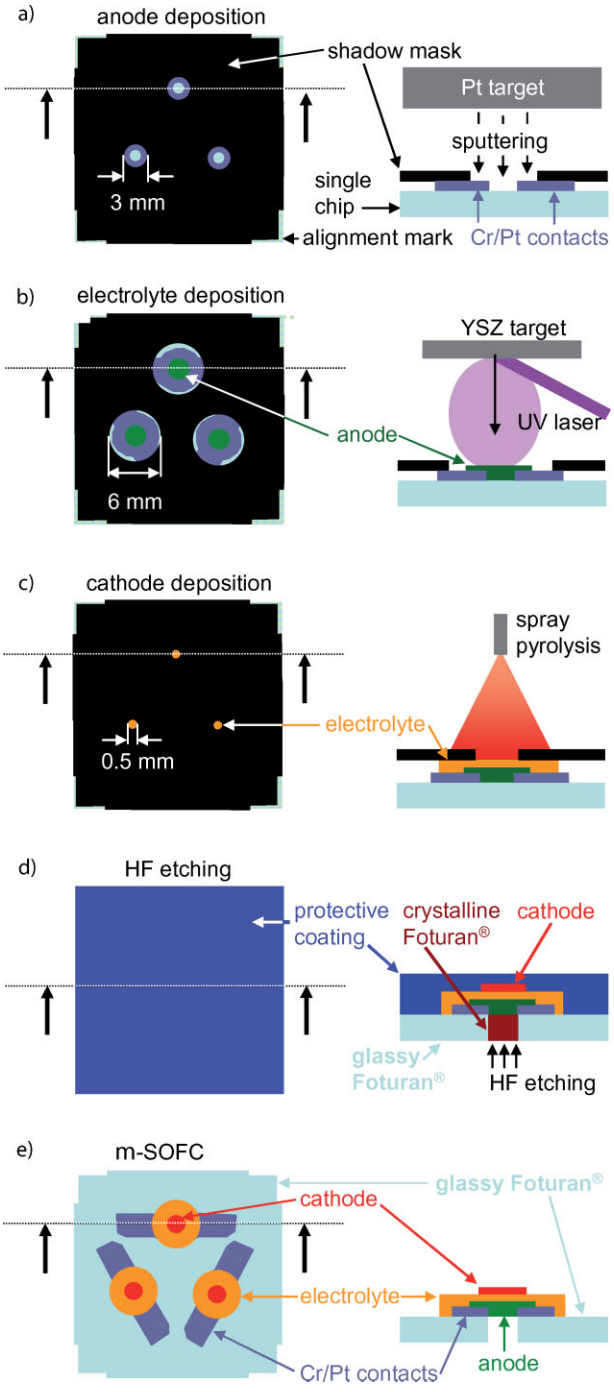

Scheme 2. Thin-film deposition through shadow masks on a single-chip substrate and back-etching of the fuel cell membranes. Top views on the left and cross-sections on the right. Drawings not to scale.

For electrochemical measurements, the cells with platinum wires attached were sandwiched between two alumina spacer rings. This assembly was mounted between two quartz glass sample holders in a tubular furnace of 65 cm length. A schematic of the setup is given elsewhere[72]. Four 1 mm-thick ceramic paper rings (Insulfrax, Unifrax, Duesseldorf, DE) were used as sealing rings and feed-throughs for the Pt contact wires between the cell and the alumina spacers, and between the spacers and the sample holder.

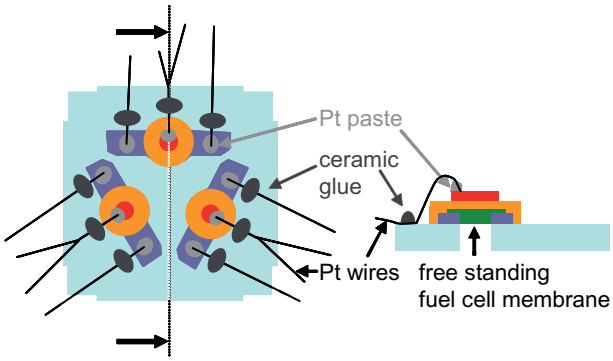

Scheme 3. Top- and cross-sectional views of a contacted cell ready for electrochemical testing. Drawing not to scale.

The cells were heated in air with 3 °C min^{-1} to the maximum testing temperature of 550–600 °C to sinter the platinum paste used for contacting and to harden the ceramic glue. The gas flow rate on the anode side was 60 sccm air and on the cathode side 300 sccm air. Air on the anode side was used to ensure a clean burning out of the organic binder of the Pt paste. All gas flows were controlled by mass flow controllers (El-Flow, Bronkhorst, Reinach, CH). After 1 h in air, the anode side was purged with 500 sccm dry nitrogen for 10–30 min and then hydrogen was added. The volumetric hydrogen to nitrogen ratio was 1:4 and the cells were measured in dry and 3 vol % humidified atmosphere on the anode side. Humidification was achieved by reacting air in the anode gas stream inside the oven over a Pt mesh. The total anode gas flow rate with and without water vapor was 500 sccm.

After 20 min under reducing conditions, the *I–V* curves of the individual cells were measured with a slew rate of 2 mV s^{-1} (IM6) and the electrochemical impedance spectra were recorded at open circuit conditions in the frequency range of 1 Hz–4 MHz with an AC amplitude of 20 mV (IM6). The cell chip was then cooled down under a reducing atmosphere at a rate of 3 °C min^{-1} and electrochemically characterized in 50–100 °C steps down to 400 °C. The data were analyzed using the ZView and CorrView software (Scribner Associates, Southern Pines, NC, USA).

A low frequency arc and a small high frequency arc above ~200 kHz were observed in the Nyquist plots of all tested cells. The high frequency arc was independent of the cathode material, DC bias or gas atmosphere at the electrodes and was attributed to the electrolyte resistance. The low frequency part of the spectrum was attributed to the electrodes. The value of the electrolyte resistance was extracted from the spectra by fitting with an equivalent circuit of two $R||$CPE circuits in series for the electrolyte and electrode, with R being a resistor and CPE a constant phase element.

Due to the geometry of the cells, not only is the fuel cell active area itself covered with the anode, electrolyte, and cathode, but also these layers extend to some area beside it (Scheme 4a). The electrochemically active region with area A_{act} is the free-standing membrane, where the anode is exposed to the fuel gas. The anode and the cathode both extend beyond the active area, creating a passive region with area A_{pas}, parallel to the active region. The active and passive cell impedances each consist of the anode, electrolyte, and cathode impedances $Z_{A,act}$, $Z_{\Omega,act}$, $Z_{C,act}$, and $Z_{A,pas}$, $Z_{\Omega,pas}$, $Z_{C,pas}$, respectively.

With impedance spectroscopy, the parallel circuit of the active and the passive parts of the cell is measured (Scheme 4b). The correct value of the area-specific electrolyte resistance R_Ω can be extracted from the impedance spectra by normalizing the electrolyte contribution of the spectrum with the sum of active and passive area $[R_\Omega = (Z_{\Omega,act} + Z_{\Omega,pas})(A_{act} + A_{pas})]$.

However, the gas atmosphere at the passive anode area is poorly defined and the anode impedance of the passive area $Z_{A,pas}$ is not equal to that of the active area $Z_{A,act}$. The apparent electrode polarization

ADVANCED FUNCTIONAL MATERIALS

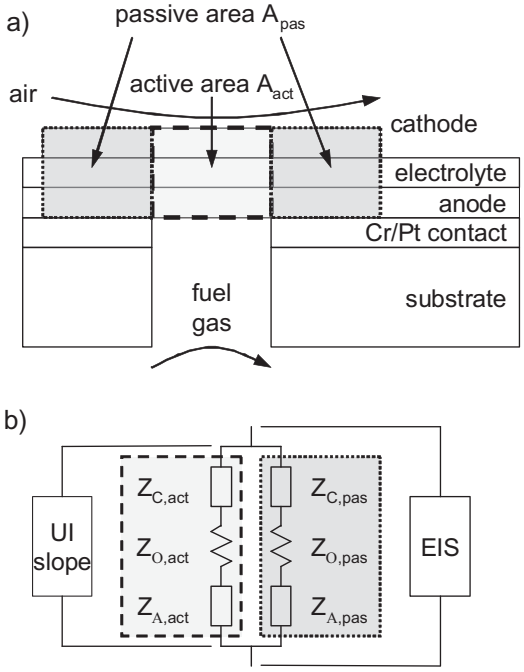

Scheme 4. Representation of the electrochemically active and passive areas in a miniaturized fuel cell (a) and the corresponding equivalent circuit (b).

resistance $(Z_{A,act}+Z_{A,pas}+Z_{C,act}+Z_{C,pas})(A_{act}+A_{pas})$ measured by impedance spectroscopy does not, therefore, correspond to the "real" polarization resistance of the electrodes $R_A+R_C=(Z_{A,act}+Z_{C,act})A_{act}$ of the active area. So, the polarization resistance of the electrodes R_A+R_C was extracted from the *I–V* curves of the cells instead. The slope of the *I–V* curve normalized to the active cell area at the open circuit condition corresponds to the sum of the anode and cathode polarization resistances R_A+R_C plus the specific electrolyte resistance R_Ω. As will be seen later, the electrolyte contribution to the overall cell resistance was negligible for all cells tested and the slope of the *I–V* curve at zero current was used as electrode polarization resistance in the following.

Consequently, the impedance raw data of the cells with platinum paste cathode were normalized to the area of the platinum paste dot, whereas in the case of the sputtered platinum and LSCF cathodes, the impedance data were normalized to the area of the sputtered platinum or LSCF.

The anode is a Pt thin film with pores that extend through the complete thickness of the film, i.e., similar to a metal foil with holes (see Fig. 1). If the anode is sandwiched between the dense electrolyte and the dense substrate material, the pores are not connected to each other and there is no gas diffusion between pores. Hydrogen can only diffuse to the triple phase boundary Pt–YSZ-pore at the position of the hole in the substrate material and an electrochemical reaction only occurs at the free-standing membrane. The current–voltage raw data of all cells were, therefore, normalized to the active fuel cell (membrane) area.

Received: May 04, 2007
Revised: March 02, 2008
Published online: September 29, 2008

[1] A. Bieberle-Hütter, D. Beckel, U. P. Muecke, J. L. M. Rupp, A. Infortuna, L. J. Gauckler, *mstnews* **2005**, *4–05*, 12.
[2] D. Nikbin, *Fuel Cell Rev.* **2006**, *4/5*, 21.
[3] H. L. Maynard, J. P. Meyers, *J. Vac. Sci. Technol, B* **2002**, *20*, 1287.
[4] C. K. Dyer, *J. Power Sources* **2002**, *106*, 31.
[5] C. W. Wong, T. S. Zhao, Q. Ye, J. G. Liu, *J. Power Sources* **2006**, *155*, 291.
[6] D. Modroukas, V. Modi, L. G. Frechette, *J. Micromech. Microeng.* **2005**, *15*, S193.
[7] G. Q. Lu, C. Y. Wang, *J. Power Sources* **2005**, *144*, 141.
[8] J. D. Morse, *Int. J. Energy Res.* **2007**, *31*, 576.
[9] G. J. La O, H. J. In, E. Crumlin, G. Barbastathis, Y. Shao-Horn, *Int. J. Energy Res.* **2007**, *31*, 548.
[10] N. T. Nguyen, S. H. Chan, *J. Micromech. Microeng.* **2006**, *16*, R1.
[11] J. Yu, P. Cheng, Z. Ma, B. Yi, *J. Power Sources* **2003**, *124*, 40.
[12] B. Sakintuna, F. Lamari-Darkrim, M. Hirscher, *Int. J. Hydrogen Energy* **2007**, *32*, 1121.
[13] A. M. Seayad, D. M. Antonelli, *Adv. Mater.* **2004**, *16*, 765.
[14] S. K. Kamarudin, W. R. W. Daud, S. L. Ho, U. A. Hasran, *J. Power Sources* **2007**, *163*, 743.
[15] D. Linden, T. B. Reddy, *Handbook of Batteries*, 3rd ed, McGraw-Hill, New York **2002**.
[16] N. Hotz, M. J. Stutz, S. Loher, W. J. Stark, D. Poulikakos, *Appl. Catal, B* **2007**, *73*, 336.
[17] F. Chen, S. Zha, J. Dong, M. Liu, *Solid State Ionics* **2004**, *166*, 269.
[18] T. Tsai, S. A. Barnett, *J. Vac. Sci. Technol, A* **1995**, *13*, 1073.
[19] G. J. La, O J. Hertz, H. Tuller, Y. Shao-Horn, *J. Electroceram.* **2004**, *13*, 691.
[20] M. L. Liu, D. S. Wang, *J. Mater. Res.* **1995**, *10*, 3210.
[21] C. Argirusis, T. Damjanovic, G. Borchardt, *Key Eng. Mater.* **2006**, *314*, 101.
[22] C.-Y. Fu, C.-L. Chang, C.-S. Hsu, B.-H. Hwang, *Mater. Chem. Phys.* **2005**, *91*, 28.
[23] I. Taniguchi, R. C. van Landschoot, J. Schoonman, *Solid State Ionics* **2003**, *156*, 1.
[24] U. P. Muecke, N. Lüchinger, L. Schlagenhauf, L. J. Gauckler, *Thin Solid Films* **2008**, in press.
[25] J. L. M. Rupp, L. J. Gauckler, *Solid State Ionics* **2006**, *177*, 2513.
[26] D. Beckel, A. Dubach, A. R. Studart, L. J. Gauckler, *J. Electroceram.* **2006**, *16*, 221.
[27] D. Beckel, U. P. Muecke, T. Gyger, G. Florey, A. Infortuna, L. J. Gauckler, *Solid State Ionics* **2007**, *178*, 407.
[28] D. Beckel, D. Briand, A. R. Studart, N. F. de Rooij, L. J. Gauckler, *Adv. Mater.* **2006**, *18*, 3015.
[29] A. B. Bieberle-Hütter, H. L. Tuller, *J. Electroceram.* **2006**, *16*, 151.
[30] J. L. Hertz, H. L. Tuller, *J. Electroceram.* **2004**, *13*, 663.
[31] L. S. Wang, S. A. Barnett, *Solid State Ionics* **1993**, *61*, 273.
[32] S. Y. Chun, N. Mizutani, *Appl. Surf. Sci.* **2001**, *171*, 82.
[33] T. Suzuki, I. Kosacki, H. U. Anderson, *Solid State Ionics* **2002**, *151*, 111.
[34] I. Kosacki, T. Suzuki, V. Petrovsky, H. U. Anderson, *Solid State Ionics* **2000**, *136–137*, 1225.
[35] G. Chiodelli, L. Malavasi, V. Massarotti, P. Mustarelli, E. Quartarone, *Solid State Ionics* **2005**, *176*, 1505.
[36] L. Chen, C. L. Chen, D. X. Huang, Y. Lin, X. Chen, A. J. Jacobson, *Solid State Ionics* **2004**, *175*, 103.
[37] C. S. Hsu, B. H. Hwang, *J. Electrochem. Soc.* **2006**, *153*, A1478.
[38] D. Beckel, D. Briand, A. Bieberle-Hütter, J. Courbat, N. F. De Rooij, L. J. Gauckler, *J. Power Sources* **2007**, *166*, 143.
[39] A. Bieberle-Hütter, M. Sogaard, H. L. Tuller, *Solid State Ionics* **2006**, *177*, 1969.
[40] J. Fleig, H. L. Tuller, J. Maier, *Solid State Ionics* **2004**, *174*, 261.
[41] N. Hotz, S. M. Senn, D. Poulikakos, *J. Power Sources* **2006**, *158*, 333.
[42] H. Huang, M. Nakamura, P. Su, R. Fasching, Y. Saito, F. B. Prinz, *J. Electrochem. Soc.* **2007**, *154*, B20.

[43] X. Chen, N. J. Wu, L. Smith, A. Ignatiev, *Appl. Phys. Lett.* **2004**, *84*, 2700.
[44] S. Kang, P. C. Su, Y. I. Park, Y. Salto, F. B. Prinz, *J. Electrochem. Soc.* **2006**, *153*, A554.
[45] M. Prestat, A. Infortuna, S. Korrodi, S. Rey-Mermet, P. Muralt, L. J. Gauckler, *J. Electroceram.* **2007**, *18*, 111.
[46] M. Prestat, J.-F. Koenig, L. J. Gauckler, *J. Electroceram.* **2007**, *18*, 87.
[47] J.-M. Bae, B. C. H. Steele, *Solid State Ionics* **1998**, *106*, 247.
[48] T. R. Dietrich, W. Ehrfeld, M. Lacher, M. Kramer, B. Speit, *Microelectron. Eng.* **1996**, *30*, 497.
[49] Mikroglas Chemtech GmbH, http://www.mikroglas.de (accessed 04.05.2007).
[50] J. Vanherle, A. J. McEvoy, *Ber. Bunsen-Ges. Phys. Chem. Chem. Phys.* **1993**, *97*, 470.
[51] R. Baker, J. Guindet, M. Kleitz, *J. Electrochem. Soc.* **1997**, *144*, 2427.
[52] N. L. Robertson, J. N. Michaels, *J. Electrochem. Soc.* **1990**, *137*, 129.
[53] A. Infortuna, A. S. Harvey, L. J. Gauckler, *Adv. Funct. Mater.* **2007**, *18*, 127.
[54] M. Sase, D. Ueno, K. Yashiro, A. Kaimai, T. Kawada, J. Mizusaki, *J. Phys. Chem. Solids* **2005**, *66*, 343.
[55] J. M. Ralph, C. Rossignol, R. Kumar, *J. Electrochem. Soc.* **2003**, *150*, A1518.
[56] X. Guo, W. Sigle, J. Fleig, J. Maier, *Solid State Ionics* **2002**, *154–155*, 555.
[57] M. Han, X. Tang, H. Yin, S. Peng, *J. Power Sources* **2007**, *165*, 757.
[58] X. Xin, Z. Lu, Z. Ding, X. Huang, Z. Liu, X. Sha, Y. Zhang, W. Su, *J. Alloys Compd.* **2006**, *425*, 69.
[59] Q. Li, T. Xia, X. D. Liu, X. F. Ma, J. Meng, X. Q. Cao, *Mater. Sci. Eng, B* **2007**, *138*, 78.
[60] D. Beckel, A. Bieberle-Hütter, A. Harvey, A. Infortuna, U. P. Muecke, M. Prestat, J. L. M. Rupp, L. J. Gauckler, *J. Power Sources* **2007**, *173*, 325.
[61] J. H. Joo, G. M. Choi, *Solid State Ionics* **2006**, *177*, 1053.
[62] E. B. Ramírez, A. Huanosta, J. P. Sebastian, L. Huerta, A. Ortiz, J. C. Alonso, *J. Mater. Sci.* **2007**, *V42*, 901.
[63] C. Kleinlogel, *Cathode Supported Thin Electrolytes and Nano Sized Ceria Solid Solutions for Solid Oxide Fuel Cells*, dissertation ETH no. 13483, Swiss Federal Institute of Technology, Zurich **1999**.
[64] A. Nagata, H. Okayama, *Vacuum* **2002**, *66*, 523.
[65] T. Tsai, S. A. Barnett, *J. Electrochem. Soc.* **1995**, *142*, 3084.
[66] S. W. Zha, C. R. Xia, G. Y. Meng, *J. Appl. Electrochem.* **2001**, *31*, 93.
[67] A. F. Jankowski, J. P. Hayes, R. T. Graff, J. D. Morse, *Mater. Res. Soc. Symp. Proc.* **2002**, *730*, V4.2.1.
[68] T. Suzuki, T. Yamaguchi, Y. Fujishiro, M. Awano, *J. Power Sources* **2006**, *160*, 73.
[69] Y. Funahashi, T. Shimamori, T. Suzuki, Y. Fujishiro, M. Awano, *J. Power Sources* **2007**, *163*, 731.
[70] P. Sarkar, L. Yamarte, H. S. Rho, L. Johanson, *Int. J. Appl. Ceram. Technol.* **2007**, *4*, 103.
[71] B. Buergler, S. Vuillemin, M. Ochsner, L. J. Gauckler, *J. Power Sources* **2006**, *171*, 310.
[72] M. B. Jörger, CuO-CGO Anodes for Solid Oxide Fuel Cells, dissertation ETH no. 15351, Swiss Federal Institute of Technology, Zurich **2004**.